Chinese Journal of
POLYMER SCIENCE

RESEARCH ARTICLE

https://doi.org/10.1007/s10118-024-3159-8
Chinese J. Polym. Sci. **2024**, *42*, 1002–1014

Corrugated Graphene Paper Reinforced Silicone Resin Composite for Efficient Interface Thermal Management

Bo-Wen Wang[a,b], Heng Zhang[a], Qing-Xia He[a], Hui-Tao Yu[a], Meng-Meng Qin[a*], and Wei Feng[a*]

[a] *Tianjin Key Laboratory of Composite and Functional Materials, School of Materials Science and Engineering, Tianjin University, Tianjin 300350, China*
[b] *International Engineering Institute, Tianjin University, Tianjin 300350, China*

Electronic Supplementary Information

Abstract With the rapid development of high-power-density electronic devices, interface thermal resistance has become a critical barrier for effective heat management in high-performance electronic products. Therefore, there is an urgent demand for advanced thermal interface materials (TIMs) with high cross-plane thermal conductivity and excellent compressibility to withstand increasingly complex operating conditions. To achieve this aim, a promising strategy involves vertically arranging highly thermoconductive graphene on polymers. However, with the currently available methods, achieving a balance between low interfacial thermal resistance, bidirectional high thermal conductivity, and large-scale production is challenging. Herein, we prepared a graphene framework with continuous filler structures in in-plane and cross-plane directions by bonding corrugated graphene to planar graphene paper. The interface interaction between the graphene paper framework and polymer matrix was enhanced *via* surface functionalization to reduce the interface thermal resistance. The resulting three-dimensional thermal framework endows the polymer composite material with a cross-plane thermal conductivity of 14.4 $W{\cdot}m^{-1}{\cdot}K^{-1}$ and in-plane thermal conductivity of 130 $W{\cdot}m^{-1}{\cdot}K^{-1}$ when the thermal filler loading is 10.1 wt%, with a thermal conductivity enhancement per 1 wt% filler loading of 831%, outperforming various graphene structures as fillers. Given its high thermal conductivity, low contact thermal resistance, and low compressive modulus, the developed highly thermoconductive composite material demonstrates superior performance in TIM testing compared with TFLEX-700, an advanced commercial TIM, effectively solving the interfacial heat transfer issues in electronic systems. This novel filler structure framework also provides a solution for achieving a balance between efficient thermal management and ease of processing.

Keywords Graphene paper; Vertically aligned structure; Cross-plane thermal conductivity; Low compressive modulus; Thermal interface material

Citation: Wang, B. W.; Zhang, H.; He, Q. X.; Yu, H. T.; Qin, M. M.; Feng, W. Corrugated graphene paper reinforced silicone resin composite for efficient interface thermal management. *Chinese J. Polym. Sci.* **2024**, *42*, 1002–1014.

INTRODUCTION

Thermal management of high-power devices is a crucial challenge in current research and industrial fields.[1,2] To effectively manage the heat generated by these devices, the development of materials with excellent thermal conductivity is necessary, particularly in the vertical direction as thermal interface materials (TIMs).[3,4] Although polymers are essential electronic packaging materials, they are typically thermal insulators with a thermal conductivity of around 0.2 $W{\cdot}m^{-1}{\cdot}K^{-1}$, severely limiting their application in high-performance devices.[5,6] The development of polymer-based composites reinforced with graphene as a filler has emerged as a prominent research topic in recent years. Because graphene itself possesses an ultrahigh thermal conductivity ranging from 3500 $W{\cdot}m^{-1}{\cdot}K^{-1}$ to 5300 $W{\cdot}m^{-1}{\cdot}K^{-1}$, surpassing traditional ceramic and metal fillers such as copper, silver, and boron.[7,8] However, it must be noted that the thermal conductivity of graphene is anisotropic,[9,10] and the graphene sheets are at the micro or nano scales, which will greatly affect the thermal conductivity of composites. There are different material preparation strategies in both industry and academia for these issues.

In industry, the incorporation of uniformly dispersed graphene fillers into polymers is a common method to produce graphene reinforced thermal conductive composites.[11,12] This approach has many advantages, such as relative simplicity in the fabrication process, lower cost, and scalability for large-scale production.[13] However, despite the inherent high thermal conductivity of graphene, its full potential is not realized due to the disordered orientation and interfacial thermal resistance of graphene sheets.[14,15] Blindly increasing the content of graphene can also easily lead to deterioration of mechanical properties such as modulus and hardness.

In the academic field, constructing directional heat conduction pathways through the vertical orientation of graphene

* Corresponding authors, E-mail: qmm@tju.edu.cn (M.M.Q.)
E-mail: weifeng@tju.edu.cn (W.F.)

Special Issue: Functional Polymer Materials
Received April 9, 2024; Accepted May 8, 2024; Published online May 23, 2024

sheets can significantly improve the utilization efficiency of graphene and the thermal conductivity of composite.[16–18] Compared to randomly arranged structures, this highly ordered graphene anisotropic structure can achieve higher thermal conductivity at lower filler loadings, thereby improving the utilization efficiency of thermal fillers.[19–21] For example, freeze casting technique offers precise control over the freezing rate and shape of the freezing template, enabling highly controllable three-dimensional graphene network structures while maintaining good mechanical strength and structural stability.[22] Yu *et al*.[23] prepared oriented three-dimensional graphene aerogels by mixing graphene oxide solution with polyacrylamide and employing a biaxial freeze-casting process. Subsequently, the aerogel underwent high-temperature annealing at 2800 °C and was compounded with paraffin, resulting in a longitudinal thermal conductivity of 8.87 $W{\cdot}m^{-1}{\cdot}K^{-1}$. Zeng *et al*.[24] applied polybutadiene coating onto surface-functionalized graphite films and employed a cross-stacking process to fabricate horizontally oriented composites. Following that, the graphite film underwent a vertical orientation by means of cutting and flipping, resulting in a remarkable through-plane thermal conductivity of 64.90 $W{\cdot}m^{-1}{\cdot}K^{-1}$. Although these methods significantly improve the utilization efficiency of graphene and have higher thermal conductivity than commercial thermal interface materials, they face the challenges of cumbersome preparation methods and difficulty in large-scale preparation.

Especially, as a thermal interface material, the contact condition between the filler and the device is crucial for its interfacial thermal resistance. Vertically oriented graphene typically comes into contact with the device through its cross-section, and the nanoscale size makes it difficult to quickly transfer heat from the device to the thermal interface material, thereby compromising thermal management performance.[25,26] Therefore, how to ensure the vertical orientation of graphene while increasing its contact area with devices and possessing the potential for large-scale processing, has become the key to the development of high-performance graphene based thermal interface materials.

Herein, we developed a feasible hot-pressing process to prepare a corrugated graphene paper (CGP) with an aligned microstructure using conventional graphene paper as starting material. Firstly, the surface of graphene paper was treated by plasma to introduce oxygen-containing functional groups, followed by the treatment of silane coupling agent. Then, CGP was constructed by hot-pressing graphene paper in a simple compression mold with periodic groove structure. Thermal conductive composite materials (CGP/PPDMS) were obtained by introducing organic silicon into the corrugated graphene paper. Due to the continuous graphene structure in both in-plane and cross-plane directions, the composites exhibit excellent thermal conductivity (130 and 14.4 $W{\cdot}m^{-1}{\cdot}K^{-1}$) and thermal conductivity enhancement efficiency (831%). The composite of flexible silicone rubber and elastic corrugated graphene gives the composites excellent soft elasticity, so its interface contact thermal resistance is as low as 52.7 $K{\cdot}mm^2{\cdot}W^{-1}$. By comparing it with advanced commercial thermal interface materials (TIMs), we further demonstrated the superior performance of our CGP/PPDMS composite material in interface heat transfer capabilities. The results of this study provide valuable insights for the construction of high-performance TIMs that has the potential for mass production.

EXPERIMENTAL

Materials

Hydride-terminated polydimethylsiloxane (HPDMS, $M_w \approx 2.4\times10^4$ $g{\cdot}mol^{-1}$), vinyl-terminated polydimethylsiloxane (VPDMS, $M_w \approx 2.8\times10^4$ $g{\cdot}mol^{-1}$), Karstedt's catalyst, and ethyl acetate (99.5% purity) were obtained from Aladdin Co., Ltd., China. 3-(Trimethoxysilyl)propyl methacrylate (TMSPMA), polydimethylsiloxane(PDMS; viscosity 500cSt, plasticizer), and ammonia water (98% purity) were purchased from Heowns Co., Ltd., China. Graphene paper (GP) with thickness of 20 μm was provided by Hefei Aoqi Electronic Technology Co., Ltd., China. All the chemicals were used as received without further purification. Deionized water was prepared in the laboratory. Quartz flakes used as the substrate were purchased from Daiermeng Science and Technology, Ltd., China. Two-component liquid silicone rubber (SYLGARD 184), consisting of liquid silicone rubber as component A and a curing agent as component B in an A:B mass ratio of 10:1, was purchased from Dow Corning, USA.

Preparation of Functional GP

GP samples with a thickness of 20 μm were cut into 4 cm × 10 cm pieces and placed in vacuum plasma treatment equipment to remove surface impurities, and etch defects, and generate oxygen-containing groups on the surface. Plasma-treated GP samples were immersed in a mixture of hydrogen peroxide (30 wt%) and ammonia water (25 wt%) (5:1, *V*:*V*) for 12 h for surface hydroxylation at 60 °C. The hydroxylated GP samples were rinsed and dried, and then placed for 24 h in vinyl silane solution. which was prepared by adding 10 mL of acetic acid (pH=3.5) and 2 wt% TMSPMA to 100 mL of deionized water, and incubating at room temperature for 5 h. Subsequently, the paper samples were washed with ethanol and dried to obtain the functionally treated GP samples.

Preparation of Plasticized Polydimethylsiloxane (PPDMS)

A specific molar ratio (*x*:*y*) of *x*-HPDMS and *y*-VPDMS, along with a small amount of ethyl acetate as a solvent, were placed in a beaker and stirred for 8 h. Subsequently, Karstedt's catalyst (5 $mg{\cdot}L^{-1}$) was added to the thoroughly mixed PDMS solution and stirred extensively. Vacuum was applied to remove bubbles, and the mixture was heated at 85 °C for 6 h. The preparation of PPDMS followed a similar procedure, with the addition of the desired proportion of silicone oil before introducing the catalyst, while maintaining the same curing temperature. Preparation of corrugated graphene paper (CGP)/PPDMS composite materials

The functional GP was pressed using a compression molding technique inside a copper mold with continuous vertical array structures at a temperature of 200 °C and a pressure of 1.0 MPa, resulting in the formation of CGP, as a thermally conductive filler. However, the resulting filler structure did not withstand most thermal sources. To address this issue, one of the horizontal planes of the filler structure was encapsulated using flat GP and super-glue. The prepared filler structure exhibited a certain level of customizability, which warrants further research. After repeated vacuum-assisted impregnation,

https://doi.org/10.1007/s10118-024-3159-8

CGP/PPDMS composite materials with different sizes of CGP were obtained. The resulting composite materials were heated at 85±1 °C for 24 h. To improve the quality of the composite material samples, a glass slide was applied to the top and bottom horizontal surfaces during curing to reduce excessive polymer-induced thermal resistance.

Characterization

The morphology and microstructure of CGP were analyzed using field-emission scanning electron microscopy on a Hitachi S4800-15 kV instrument. The surface chemical compositions were determined using X-ray photoelectron spectroscopy (XPS; K-Alpha$^+$, Thermo Fisher, USA). Fourier transform infrared (FTIR) spectra were recorded on a Thermo Scientific Nicolet iS20 spectrometer using 32 scans from 3500 cm^{-1} to 500 cm^{-1}. Compression and shear strength tests were performed on the composites using a general mechanical testing machine (XQ-1C, Xi'an, China). In this case, the compression rate was 2 mm·min^{-1} and the specimen size was 20 mm (length) × 20 mm (width) × 2 mm (height). The shear rate was 5 mm·min^{-1} and the specimen size was 10 cm (length) × 1.5 cm (width) × 4 mm (height). The thermal diffusivity (α) was measured using a laser flash apparatus (LFA 467, Netzsch, Germany), and the specific heat capacity (C_p) was measured using a differential scanning calorimeter (DSC; Q20, TA Instruments, USA), and the density (ρ) was determined using the water displacement method. Thermogravimetric analysis (TGA) curves were obtained on an STA 449F3 instrument in the temperature range from 30 °C to 800 °C at a heating rate of 10 °C·min^{-1} under a dry nitrogen atmosphere. In addition, the compressive thermal conductivity was measured using the heat flux method (TC2120E, XIATECH, China) with a sample size of Φ 25 mm × 2 mm. Infrared (IR) images were obtained using a Fluke TiX640 IR camera to record the temperature distribution of the samples. The thermal conductivity (κ, W·m^{-1}·K^{-1}) was calculated using the following equation:

$$\kappa = \rho \cdot C_p \cdot \alpha \quad (1)$$

RESULTS AND DISCUSSION

Fig. 1(a) shows the preparation process of the CGP/PPDMS composite material with a continuously corrugated structure and flexible elasticity. The interface bonding between the GP and polymer matrix plays a crucial role in the mechanical and thermal performance of TIMs.[27,28] Therefore, we enhanced the interface bonding by functionalizing the GP surface, *via* two main steps: plasma treatment and grafting of TMSPMA. The as-obtained functionalized GP (F-GP) can be used to prepare CGP thermal conductive fillers with a specific corrugated structure using a simple compression molding method at a specific temperature and pressure. Subsequently, we integrated CGP with PPDMS by performing multiple vacuum-assisted impregnation steps to form the CGP/PPDMS composite material. The special corrugated structure of the thermally conductive filler provides an effective heat conduction pathway within the composite material, while PPDMS exhibits a low elastic modulus and excellent resilience, resulting in improved mechanical properties and reduced interface thermal resistance owing to the stable chemical bonding between both composites.[24] As shown in Fig. S1 (in the electronic supplementary information, ESI), the size of the thermally conductive filler could be adjusted according to the dimensions of the mold used, which provided a certain degree of customization. As shown in Fig. 1(b), we constructed five regular, adjustable thermal conductive oriented structures, with different radius (R) and named them $R1$ to $R5$, where $R1$ has the most compact oriented structure and $R5$ has the sparsest oriented structure. The physical images clearly demonstrate good and regular bonding between the thermally conductive fillers and the polymer matrix. The unique corrugated structure of CGP-R fillers, along with the diverse spatial structure formed after integration with the matrix, can be expected to influence the thermal and mechanical performance of the resulting composite material.

The matrix material used in this study was prepared *via* the hydrosilylation reaction between VPDMS and platinum-catalyzed HPDMS, which is a commonly used crosslinking reaction in the synthesis of organosiloxane elastomers.[29] Due to the functional groups located at the ends of the PDMS prepolymers, the crosslinked chains exhibit physical entanglement rather than covalent bonding between multiple polymer chains. To enhance the flexibility of the material, we added dimethyl silicone oil as a nonreactive plasticizer to the silicone rubber system. As shown in Fig. 1(c), the crosslinking reaction between HPDMS and VPDMS in an x:y ratio is conducted at 85 °C, leading to molecular chains with different lengths within the polymer, which influenced the compression performance. The plasticizer content refers to the mass ratio of the overall matrix material.

The cross-sectional SEM images of the microstructure of GP (Figs. 1e and 1f) show a dense multilayer structure with a thickness of 20 μm upon magnification. During the experimental process, we found that conventional compression molding methods were ineffective for converting GP into CGP, resulting in a certain degree of collapse. However, interestingly, this problem could be overcome by using appropriate temperature and pressure conditions (200 °C and 1.0 MPa) during the compression molding process, allowing the GP to be effectively shaped without collapse. This phenomenon is explained from a microscopic point of view, as shown in Figs. 1(g) and 1(h). Even though the graphene paper has already possessed a relatively thin thickness (20 μm), the manifestation of the force on its upper and lower surfaces during compression is still different. In particular, the location of the trough of the corrugated-type structure, with its upper layer close to the pressure source, is mainly affected by compression, while the lower layer is far away from the pressure source and is mainly affected by tensile action. If the applied compressive force is too large, it can produce the generation of irreversible microfolds and lead to the occurrence of layer separation.[30,31] Fig. 1(d) depicts a schematic representation of the deformation during the GP shaping process, in which a reversible plastic deformation is induced by applying a compressive force, where the applied compressive force induces a rearrangement of atoms within the graphene paper material. By applying an appropriate compression force, the interlayer spacing of the graphite sheet can be gradually reduced to form the desired corrugated structure. At the same time, higher temperatures increase the thermal movement of the material's molecules, providing a greater amount of thermal

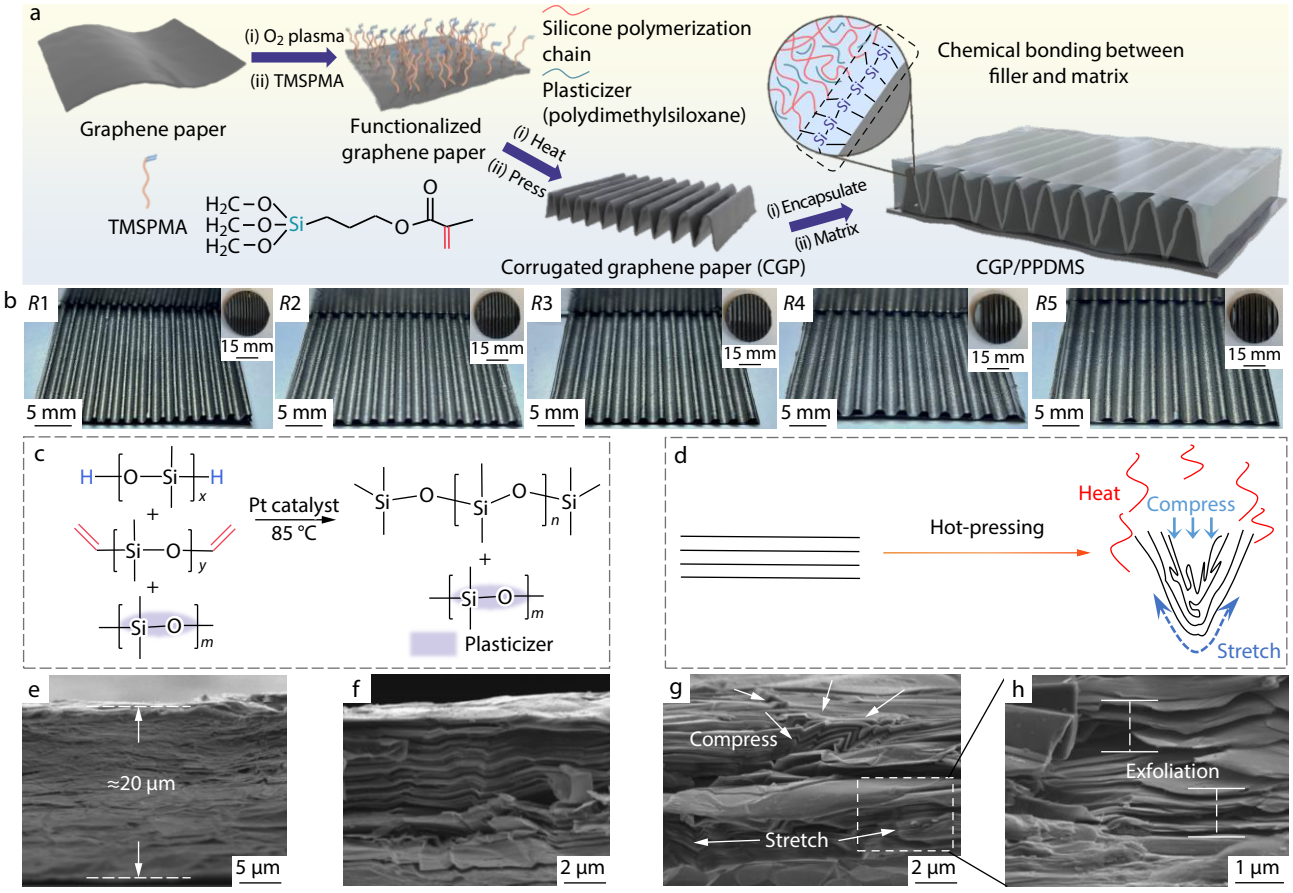

Fig. 1 Preparation process of the corrugated graphene paper (CGP)/plasticized polydimethylsiloxane (PPDMS) composite material. (a) Schematic of the preparation of the CGP/PPDMS composite material; (b) Physical images of thermally conductive fillers of different radius (*R*) and their composites; (c) Polymer formation *via* hydrosilylation; (d) Schematic representation of the deformation of the trough position when the temperature effect is introduced in the molding process; (e, f) SEM images of the cross-section of graphene paper; (g) The upper and lower layers at the trough position of the GP are affected by compression and tension, respectively; (h) Generation of layer separation.

energy and making displacement between molecules more likely to occur. This increase in thermal energy helps to alleviate the stress concentration phenomenon, thus reducing the stress aggregation effect during plastic deformation.

The principle of silane coupling agent grafting onto the surface of GP is depicted in Fig. 2(a). Initially, the relevant groups in the silane coupling agent underwent hydrolysis, resulting in the formation of silanols. Subsequently, these silanols interacted with the hydroxyl groups on the GP surface, forming hydrogen bonds and undergoing condensation reactions. Simultaneously, the silanols interlink and aggregate to form a network-like structure. The hydrophobic groups on the outer side of the silane coupling agent enhance compatibility with the polymer and expose the reactive double bonds for addition reactions. The functionalization of GP alters its surface properties, which can be evaluated using the change in water contact angle as an indicator, as shown in Fig. 2(d). The contact angle of the original GP was 82.7°, indicating neither hydrophobic nor hydrophilic characteristics. After plasma treatment, the contact angle of GP decreased to 22.7°, which is indicative of strong hydrophilicity attributable to the introduction of numerous oxygen-containing groups on the GP surface due to plasma bombardment.[32,33] Meanwhile, the contact angle of GP after coupling agent grafting increased to 108.4°, indicating strong hydrophobicity, which stems from TMSPMA with hydrophobic characteristics successfully covering the GP surface. As shown in Fig. S2(a) (in ESI), compared with GP, the XPS spectrum of F-GP showed a silicon peak, indicating the successful grafting of TMSPMA onto the GP surface. This demonstrates the formation of a chemical bond between TMSPMA and GP, thus achieving functionalization. Additionally, the relative elemental composition of carbon, silicon, and oxygen in GP before and after treatment was quantitatively analyzed by XPS (Fig. S2b in ESI). The results revealed a substantial increase in the oxygen/carbon atomic ratio in F-GP, suggesting that the functionalization treatment introduced more oxygen atoms, which altered the chemical composition of GP. These changes further confirmed the success of functionalization. The FTIR spectra of the PPDMS matrix and CGP/PPDMS composite material were recorded to evaluate the interfacial interactions between the two components. The FTIR spectra shown in Fig. S3 (in ESI) exhibit a redshift phenomenon, implying a strong interface bonding. The redshift phenomenon can be attribut-

https://doi.org/10.1007/s10118-024-3159-8

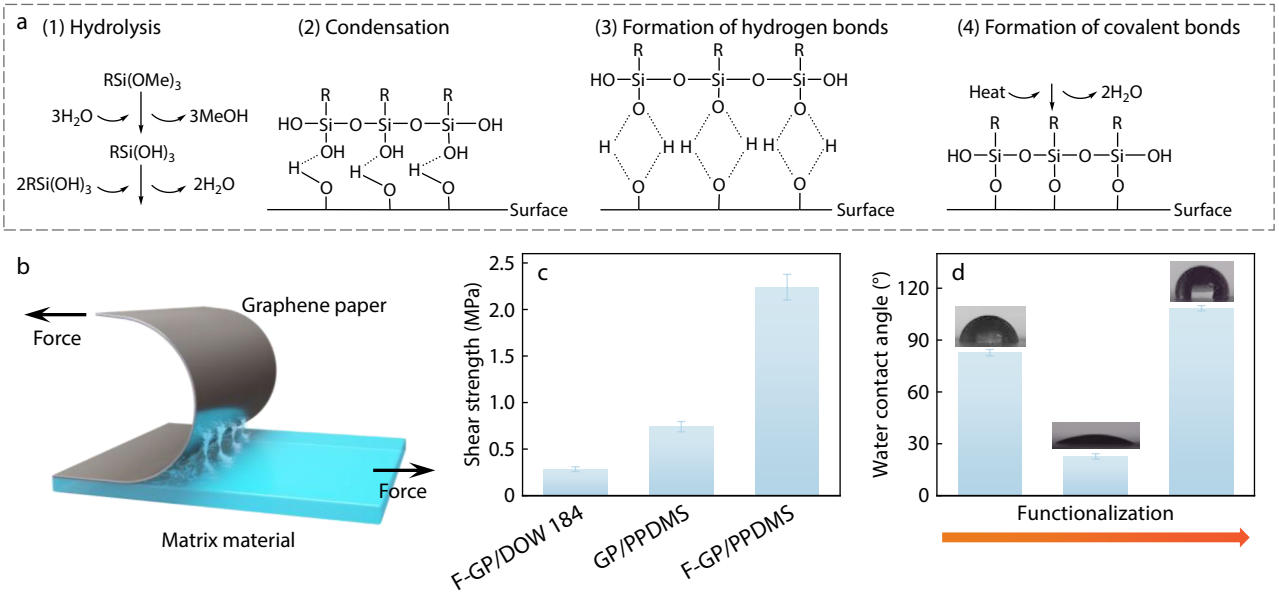

Fig. 2 Surface treatment of graphene paper (GP) and its impact on the interfacial strength. (a) Hydrolysis mechanism of the silane coupling agent; (b) Schematic of the shear strength test; (c) Interfacial strength of three samples: functionalized GP (F-GP)/DOW 184, GP/PPDMS, and F-GP/PPDMS; (d) Water contact angle of the GP surface.

ed to enhanced intermolecular interaction forces, leading to a decrease in the frequency of the vibrational modes.[34] However, this observation is merely indicative and requires further experiments and analysis to determine the exact nature and strength of the interface bonding.[3,24] To determine the interfacial bond strength, shear strength tests were conducted on samples with different interfacial states (F-GP/DOW 184, GP/PPDMS, and F-GP/PPDMS), as shown in Fig. S4 (in ESI) and Fig. 2(b). According to the data shown in Fig. 2(c), the interfacial strength of the three samples increased in the following order: F-GP/DOW 184 (0.28 MPa) < GP/PPDMS (0.74 MPa) < F-GP/PPDMS (2.24 MPa). This indicates that the PPDMS matrix exhibits considerably stronger chemical bonding with F-GP and a slightly weaker physical adhesion with the nonfunctionalized GP. This fully demonstrates the necessity of the functionalization of GP.

We investigated the mechanical properties of *x*:*y*-PDMS crosslinked polymers obtained *via* simple chain crosslinking of *x*-HPDMS and *y*-VPDMS at different molar ratios and compared them with those of the commercially available Dow184 (10:1) system. Fig. 3(a) demonstrates that 3:1-PDMS exhibited a compressive strain of up to 64% at 1 MPa, whereas Dow184 (10:1) only achieved a compressive strain of 38%. Interestingly, with an increasing *x*:*y* ratio, the maximum compressive strain of *x*:*y*-PDMS initially increased and then decreased. As shown in Fig. 3(f), the compressional modulus of the polymers and the Dow184 reference sample were calculated for six different polymerization ratios, finding that the compressional modulus and maximum compressive strain of the polymers exhibit an inverse relationship. This pattern of change can be explained as follows. First, when the cross-linking ratio is low, the number of cross-linking points of the reaction is relatively small. In this case, the cross-linking structure of the material is looser and the intermolecular interactions are weaker.[35,36] Then when more *x*-HPDMS prepolymers are introduced, their relative content increases, which reduces the modulus of the system in the form of small molecules, making the material prone to deformation and compression.[37] However, as more *x*-HPDMS prepolymers are introduced, this encourages self-cross-linking to occur and the number of cross-linking points increases. This causes the crosslinked network to begin to form a denser structure with tighter connections between the crosslinked points, enhancing the interaction forces. As a result, the material is more rigid and has an increased ability to resist deformation. As the relative content of *x*-HPDMS increases, the maximum compressive strain of *x*:*y*-PDMS shows an increasing and then decreasing trend, while the compressive modulus shows the opposite trend. The analysis of the maximum compressive strain and compressional modulus indicated that 3:1-PDMS exhibited the best compressional performance. To overcome the negative impact of the fillers on the mechanical properties, we incorporated dimethyl silicone oil as a plasticizer into the 3:1-PDMS polymer system. As shown in Fig. 3(b), under 1 MPa pressure, the addition of the plasticizer at different ratios (10 wt%–60 wt%) to the 3:1-PDMS system increases the maximum compressive strain. Furthermore, the calculation of the compressional modulus of the polymer systems with six different plasticizer contents and the 3:1-PDMS sample without plasticizer (Fig. 3c) revealed that the compressional modulus gradually decreased, indicating a considerable plasticizing effect of dimethyl silicone oil. The dimethyl silicone oil does not participate in chemical reactions within the polymer system but forms a solid solution. Its main function is to swell and increase the distance between silicone rubber molecular chains, reducing the intermolecular forces and enhancing the flexibility of the silicone rubber chains, thereby reducing the compressional modulus.[38] However, further increasing the

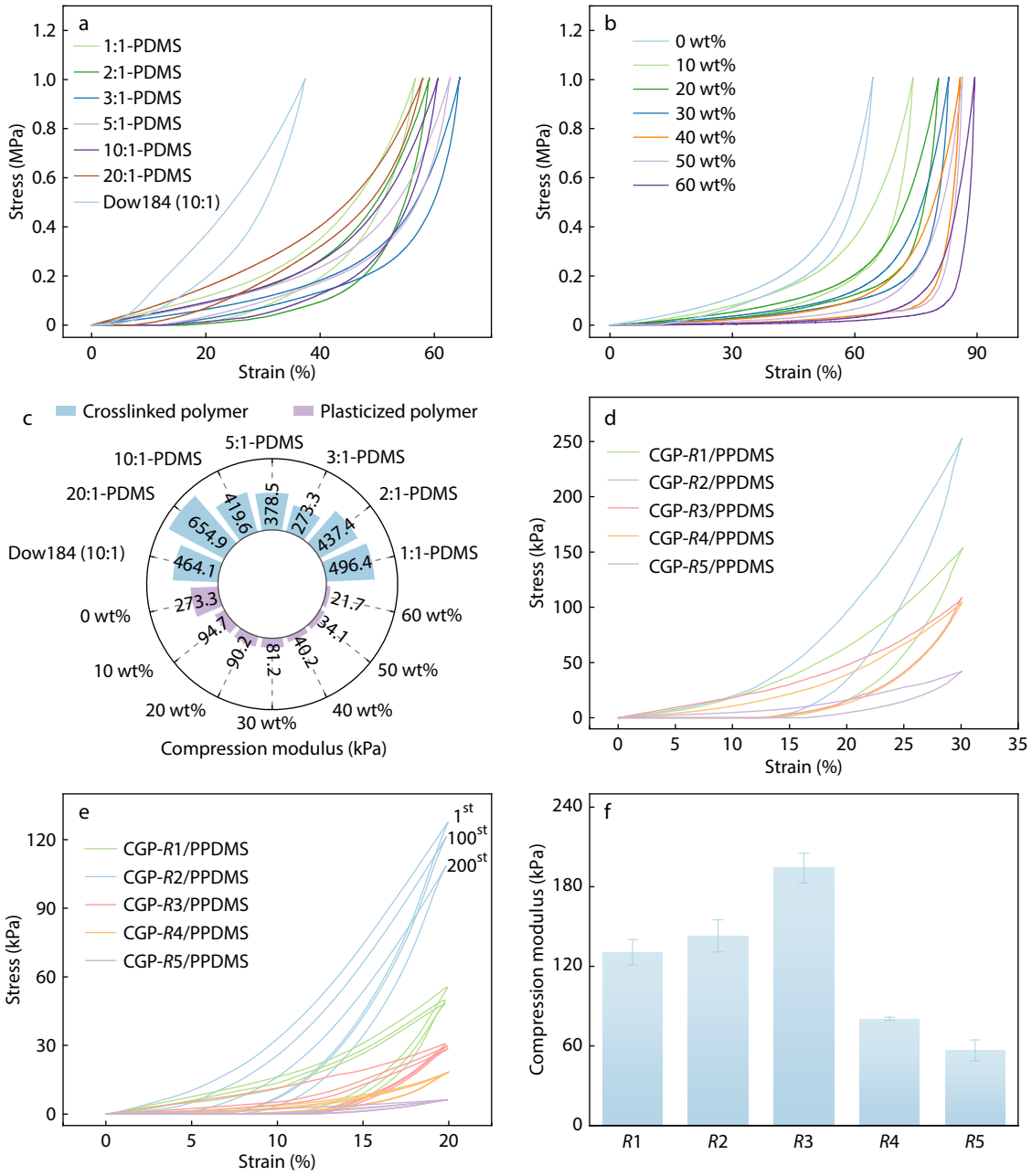

Fig. 3 Mechanical properties of *x*:*y*-PDMS, PPDMS polymer, and CGP-*R*/PPDMS composite material. (a) Stress-strain curves of *x*:*y*-PDMS crosslinked polymers with different ratios and the reference sample DOW 184; (b) Stress-strain curves of the 3:1-PDMS crosslinked polymer after plasticization treatment with a plasticizer content ranging from 10 wt% to 60 wt%; (c) Comparison of the compressional modulus of *x*:*y*-PDMS crosslinked polymers with various ratios and PPDMS; (d) Stress-strain curves of the CGP-*R*/PPDMS composite materials; (e) Stress-strain hysteresis curves of the CGP-*R*/PPDMS composite materials (200 cycles at a strain of 20%); (f) Compressional modulus of the CGP-*R*/PPDMS composite materials.

plasticizer content results in oil permeation issues within the polymer system (Fig. S5 in ESI). Oil permeation can have negative effects on material applications, such as reduced thermal conductivity, contamination of electronic devices, and decreased lifespan and reliability.[39] Therefore, we selected a 3:1-PDMS polymer system with a 30 wt% plasticizer content as the matrix for the composite material. This polymer system exhibited no oil leakage issues and achieved a maximum compressive strain of 83% (at 1.0 MPa) and a compressional modulus as low as 81.2 kPa. Fig. S6 (in ESI) illustrates the compressional cyclic performance of 3:1-PDMS and 3:1-PPDMS at 60% and 80% compressive strains. Even under high-strain levels and after 1000 compression cycles, both 3:1-PDMS and 3:1-PPDMS demonstrated good cyclic stability, indicating excellent elastic recovery and stability for application under high-strain conditions.[25] Furthermore, 3:1-PPDMS exhibits

lower stress attenuation than 3:1-PDMS, indicating that the plasticized polymer system maintained relatively stable internal connections or molecular structures during cyclic loading without significant structural fatigue or fracture. This further suggests that the plasticized polymer system possesses improved elastic recovery, stability, and durability while maintaining better mechanical performance stability under cyclic loading conditions.

We further evaluated the compressive and cyclic performance of a series of CGP-*R*/PPDMS composite materials. When compressing the composite materials to a strain of 30%, the change in the filler structure resulted in variations in the applied stress, as shown in Fig. 3(d). Except for CGP-*R*2/PPDMS, the stress of the other composite materials decreased as the array structure became sparser. This can be explained considering that the composite materials had the same size (40 mm × 40 mm × 2 mm), but the filler shapes were different, leading to variations in the volume fraction of the PPDMS matrix, which considerably influenced the mechanical properties of the composite materials. To better explain the influence of fillers on composite material performance, we used the concept of heat transfer unit (HTU). HTU refers to each repeating unit in the regular corrugated structure, as shown in Fig. 4(a). Specifically, the number (*n*) of HTUs in the five *CGP-R*/PPDMS composites can be determined from Fig. 1(b) or SP1, which are 38, 30, 26, 22 and 20, respectively. The theoretical volume (*V*, mm^3) of the matrix in CGP-*R*/PPDMS can be calculated by the radius (*R*) of the HTUs, using the following formula:

$$V = n \times S \times D = n \times D \times \left[\frac{1}{2}\pi R^2 + 2R \times (H - R) + 2 \times \left(R^2 - \frac{1}{4}\pi R^2\right)\right] = 2nDHR \quad (2)$$

where *S* denotes the cross-sectional area in the thickness direction; *n* denotes the number of HTUs; *D* denotes the width of the sample; and *H* denotes the thickness of the sample. According to Eq. (2), the theoretical volume *V* of the matrix of the CGP-*R*/PPDMS composite is related to its *R* and *n* of HTUs, and *S*, *n*, *D*, *H* and *R* are known quantities, which can be further calculated from Eq. (2), and the trend is shown in Fig. 4(a).

CGP-*R*2/PPDMS exhibits a higher compression modulus (143 kPa, Fig. 3f) and is harder to be compressed because it has a smaller *V*, which is not enough to compensate for the greater stiffness introduced by the dense corrugated structure. On the contrary, CGP-*R*5/PPDMS has a larger *V* and at the same time its sparse corrugated structure makes it less rigid, thus exhibiting a lower compression modulus and better compressibility.

It is noteworthy that the compression moduli of CGP-*R*4/PPDMS and CGP-*R*5/PPDMS (80.4 and 56.6 kPa, respectively) were lower than those of the PPDMS matrix (81.2 kPa). This may be due to the fact that corrugated-type filler has a high stiffness, which introduces higher stiffness regions in the composite, thus reducing the overall compression modulus. In addition, the corrugated-type filler structure has a large surface area and continuity. The geometry of the filler increases the interfacial area within the composite, resulting in an inhomogeneous stress distribution at the interface. This inhomogeneous stress distribution negatively affects the overall stiffness of the composite, which reduces the compression modulus. Fig. 3(e) displays the performance of the composite materials during 200 compression cycles at a strain of 20%, showing a similar trend to that of the maximum compression strain. Notably, apart from the higher compressive stress, CGP-*R*2/PPDMS also exhibited a relatively large stress attenuation (16.67 kPa). However, within the range of typical packaging pressures (lower than 2 MPa), it still demonstrated reliable mechanical cyclic performance.[21,25] This can be attributed to the excessively high rigidity of the fillers and the relatively low content of the matrix. As shown in Fig. S7 (in ESI), the CGP-*R*/PPDMS composite materials can recover their original shape after being compressed to the maximum strain, which meets the mechanical performance requirements of commercial TIMs. Overall, this material possesses excellent flexibility and an ultra-low elastic modulus, which render it adaptable to adapt to complex surface structures and ensure sufficient filling of the gaps on the contact surface under low assembly pressure, effectively reducing the contact thermal resistance (R_c).[24]

Subsequently, we studied the thermal conductivity performance of five CGP-*R*/PPDMS composite materials. To simplify the illustrations, we used the radius *R* to represent the respective CGP-*R*/PPDMS composites. Fig. 4(a) presents several factors influencing the thermal conductivity performance of the composites. The enhanced thermal conductivity of the corrugated oriented structure may be related to the contact surface area (CS, mm^2). This is due to the corrugated shape of the otherwise flat graphene layer, which means that more of the graphene layer can directly contact the surrounding environment or other materials, effectively improving the efficiency of heat transfer. And the value of CS can be calculated by multiplying the total length of GP by its width. The specific formula is as follows:

$$CS = L \times D = [2\pi R + 2 \times (H - 2R)] \times n \times D = (2\pi - 4)nDR + 2nHD \quad (3)$$

where *L* is the total length of the packing. According to Eq. (3), the contact surface area CS is also a function about *R* and *n*, and its trend is shown in Fig. 4(a). The design of the corrugated graphene thermal conductive framework realizes the construction of the thermal conductive path, and its thermal conductive path length (TP, mm) can be calculated by the following equation:

$$TP = \pi R + H - 2R = (\pi - 2)R + H \quad (4)$$

According to Eq. (4), the thermally conductive path length TP is a function about *R* and increases as *R* increases. It indicates that the larger the radius of the corrugated structure, the less favorable the heat transfer. The combined effect of these factors (*V*, CS, TP) leads to the difference in thermal conductivity between CGP-*R*/PPDMS composites with different corrugation radius. In addition, the filler loading ω can be determined from the experimentally determined filler mass percentage.

Fig. 4(b) illustrates the in-plane and through-plane thermal conductivities of the five CGP-*R*/PPDMS composite materials. Despite variations in corrugation sparsity, the in-plane thermal conductivity remained approximately constant at approximately 130 $W \cdot m^{-1} \cdot K^{-1}$. This can be attributed to the regular attachment of GP fillers on the bottom plane of the mate-

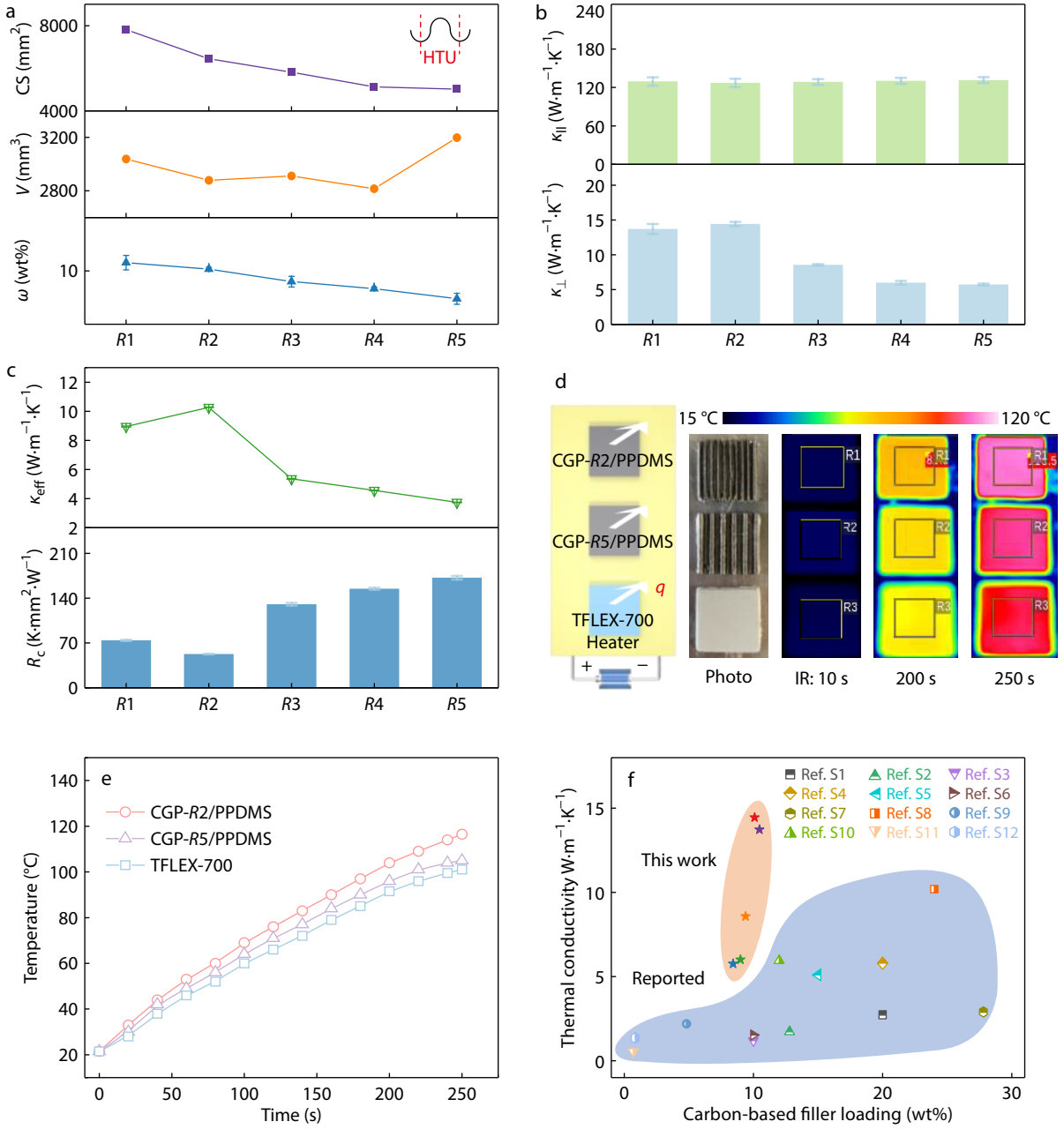

Fig. 4 Thermal performance of CGP-*R*/PPDMS composite materials. (a) Relationship between the contact surface area of the filler, the theoretical volume of the matrix and the filler loading and the radius of the corrugated structure *R*; (b) In-plane ($\kappa_{||}$) and through-plane ($\kappa_{\perp}$) thermal conductivity of the CGP-*R*/PPDMS composites; (c) Effective thermal conductivity (κ_{eff}) and interface thermal resistance (R_c) of the CGP-*R*/PPDMS composites; (d) Schematic of the planar heat transfer capability test on CGP-*R*2/PPDMS, CGP-*R*5/PPDMS and the reference sample TFLEX-700 and the corresponding infrared thermograms; (e) Temperature-time curves of the surface temperature variation for CGP-*R*2/PPDMS, CGP-*R*5/PPDMS and TFLEX-700; (f) Comparison between our composite materials and previously reported thermal materials regarding the filler loading and through-plane thermal conductivity.

rial. However, the through-plane thermal conductivity varies with the change in *R*, with CGP-*R*2/PPDMS exhibiting the highest value (14.4 $W \cdot m^{-1} \cdot K^{-1}$) and CGP-*R*5/PPDMS showing the lowest value (5.8 $W \cdot m^{-1} \cdot K^{-1}$). Interestingly, the through-plane thermal conductivity of CGP-*R*1/PPDMS, which had the most densely packed array structure, was lower than that of CGP-*R*2/PPDMS. This could be due to the higher volume fraction of the matrix in CGP-*R*1/PPDMS, which negatively affected the thermal conductivity of the material. Meanwhile, CGP-*R*2/PPDMS achieved the highest through-plane thermal conductivity owing to its denser thermal array structure and lower matrix volume fraction. Additionally, theoretical calculations revealed that TP increased as the thermal corrugated structure became sparser. The combined effect of a sparse

https://doi.org/10.1007/s10118-024-3159-8

thermal corrugated structure and a higher matrix volume fraction hinders heat transfer, leading to a gradual decrease in the through-plane thermal conductivity of CGP-*R*3/PPDMS. Compared with randomly dispersed thermal fillers, the regular, highly conductive corrugated structure used in this study provides a directional and continuous thermal path that facilitates phonon transmission.[40] By optimizing the interface state between the fillers and matrix, we successfully improved the scattering of phonons at the interface, resulting in a substantial enhancement of the thermal conductivity of the composite materials. These results demonstrate that the CGP-*R*2/PPDMS sample exhibited high thermal conductivity in both in-plane and through-plane directions. However, apart from the high thermal conductivity, the R_c of the material also plays a crucial role in the heat conduction process because it directly affects the rate and efficiency of interfacial heat transfer, which is essential for the application of thermal materials.[21] Fig. 4(c) presents the effective thermal conductivity (κ_{eff}) and R_c of the Cu/CGP-*R*/PPDMS composite material/Cu interface under a pressure of 0.1 MPa. R_c was calculated using the following formula:

$$R_c = R_{interface} - R_{bulk} = BLT/\kappa_{eff} - BLT/\kappa_{bulk} \quad (5)$$

where BLT represents the thickness between Cu layers, κ_{eff} denotes the effective thermal conductivity of the sample, and κ_{bulk} represents the intrinsic thermal conductivity of the sample. As shown in Fig. 4(c), CGP-*R*2/PPDMS achieves the lowest R_c (52.7 K·mm^2·W^{-1}) due to its denser thermal corrugated structure and stronger interfacial interactions (the specific calculation process and parameters are detailed in Table S1 in ESI). Conversely, CGP-*R*5/PPDMS exhibits a high R_c value (172.1 K·mm^2·W^{-1}) owing to its sparse thermal orientation structure and the considerable amount of polymer on its surface, which hinders the heat transfer between the two interfaces. This behavior is consistent with the trend observed for the through-plane thermal conductivity, indicating the influence of the polymer matrix on the structured thermal filler. Despite the high R_c value of 172.1 K·mm^2·W^{-1}, the unique structure of the CGP-*R*/PPDMS composite materials still exhibits good thermal conductivity. This can be attributed to the chemical bonding at the material interfaces and physical adhesion to the rough surface.[41] According to the formula $R_c = R_{total} - R_{bulk} = BLT/\kappa_{eff} - BLT/\kappa_{bulk}$, an increase in κ_{eff} effectively reduced R_{total}. To further demonstrate the excellent thermal conductivity performance of the CGP-*R*/PPDMS composite materials, we calculated the thermal conductivity enhancement (TCE) coefficient using the following formula:[42]

$$TCE = (\kappa_c - \kappa_m)/\kappa_m \times 100\% \quad (6)$$

where κ_c represents the thermal conductivity of the composite material and κ_m represents the thermal conductivity of the matrix material. The CGP-*R*2/PPDMS composite material has a TCE of 831% per 1 wt% filler loading. To further characterize the outstanding thermal conductivity performance of CGP-*R*/PPDMS, we visually compared the in-plane heat transfer capabilities of CGP-*R*2/PPDMS, CGP-*R*5/PPDMS, and a commercially advanced TIM (TFLEX-700, 5 W·m^{-1}·K^{-1}) using a thermal IR camera. As shown in Fig. 4(d), CGP-*R*2/PPDMS, CGP-*R*5/PPDMS, and TFLEX-700 of the same size and thickness (20 mm × 20 mm × 2 mm), were placed on a heater and heated simultaneously from room temperature. To ensure accurate simultaneous surface temperature measurements of the three different samples using the thermal IR camera, a thin layer of graphene was coated on top of each sample to ensure the same IR emissivity. Fig. 4(e) displays the variation of the final surface temperature with the heating time for the three samples. Compared with TFLEX-700, CGP-*R*2/PPDMS and CGP-*R*5/PPDMS exhibited faster temperature rise rates and consistently displayed slightly higher values (*e.g.*, ΔT=15.5 and 4 °C at 250 s, respectively). CGP-*R*2/PPDMS experienced faster heating owing to its higher through-plane thermal conductivity. Although the through-plane thermal conductivity of CGP-*R*5/PPDMS was slightly higher than that of TFLEX-700, there was no significant difference in the surface temperature, which may be due to the influence of interfacial thermal resistance. Fig. 4(f) compares the filler loading and through-plane thermal conductivity of the CGP-*R*/PPDMS composite material with those of previously reported carbon material/polymer composites (Table S2 in ESI). Our proposed CGP-*R*/PPDMS composite material exhibits a unique corrugated structure that enhances considerably the thermal conductivity of the polymer. The CGP-*R*/PPDMS composite materials prepared in this study combined high thermal conductivity, high elasticity, low modulus, excellent thermal stability (Fig. S9 in ESI) and low contact thermal resistance, making them promising candidates for TIMs under complex operating conditions. Additionally, composite materials possess unique customizability and can be fabricated on a large scale using a simple process, laying the foundation for practical applications.

The high through-plane thermal conductivity of CGP-*R*2/PPDMS material renders it a promising high-performance TIM for efficient heat transfer across the heater-heat sink interface. To confirm its performance, we developed a validation system simulating the thermal dissipation process of electronic components, as shown in Fig. 5(a), and compared it with TFLEX-700. In this system, CGP-*R*2/PPDMS and TFLEX-700 with dimensions of 20 mm × 20 mm × 2 mm were placed between a ceramic heater and heat sink with a bonding layer thickness (BLT) of 2 mm and a vertical pressure of 100 psi and the variation of the heater temperature was recorded. As shown in Fig. 5(b), the heater (30 W) rapidly increased in temperature after 40 s of activation and eventually reached a steady state. Clearly, CGP-*R*2/PPDMS as a TIM outperformed the TFLEX-700 thermal pad in terms of cooling performance, with a temperature drop of 70 °C at 500 seconds compared with the case without TIM (43 °C for TFLEX-700). Fig. 5(c) shows the relationship between the saturation temperature of the heater and the applied power (with and without TIM), resulting in calculated heat dissipation rates of 0.23 W/°C (no TIM), 0.34 W/°C (TFLEX-700), and 0.47 W/°C (CGP-*R*2/PPDMS). This indicates an improvement in the cooling efficiency by 104.3% and 38.2% for CGP-*R*2/PPDMS compared with the systems without TIM and with the TFLEX-700 thermal pad, respectively. Next, using finite element analysis software (COMSOL), we performed a thermal analysis of the test configuration under a rated power of 30 W and estimated κ_{eff} (Fig. 5d) for both TIMs under the same measurement conditions (detailed modeling parameters and material properties as well as the calculation procedure are shown in Tables S3, S4 and S5 in ESI). Using the κ_{eff} values of CGP-*R*2/PPDMS (*ca.* 10.7 W·m^{-1}·K^{-1}) and TFLEX-700 (~4.2 W·m^{-1}·K^{-1}), the R_c (both sides) of CGP-*R*2/PPDMS (48 K·mm^2·W^{-1}) was calculated to be

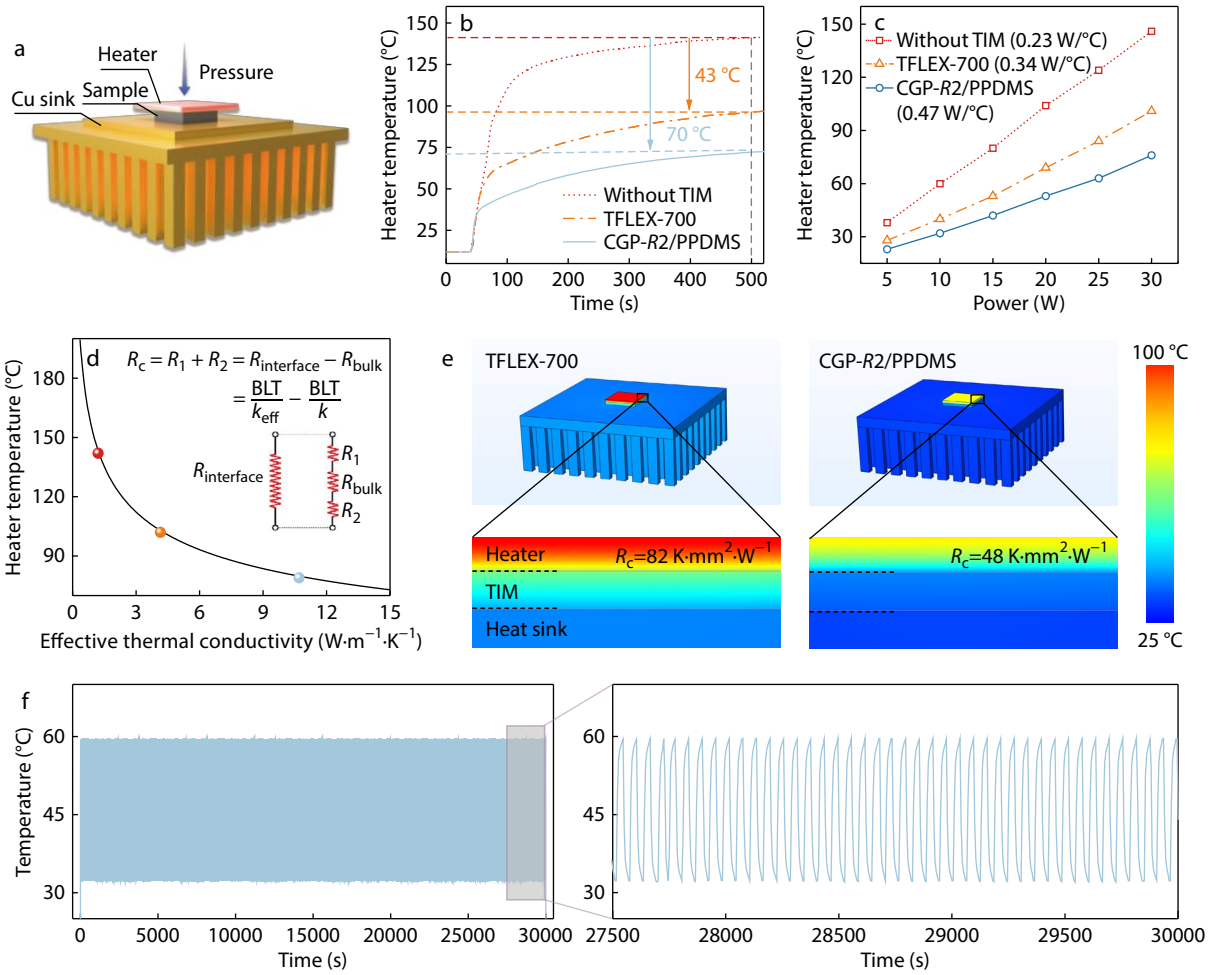

Fig. 5 Thermal management performance of CGP-*R*2/PPDMS. (a) Schematic of the setup using a thermal interface material (TIM) to bridge the heater and the heat sink; (b) Variation of the heater surface temperature with heating time in different TIM heat dissipation systems; (c) Heat-dissipation efficiency fitted from the steady-state surface temperature of the heater for different TIM heat-dissipation systems at different power levels; (d) Simulated heater temperature as a function of the effective thermal conductivity; (e) Comparison of simulated heat dissipation capabilities of different TIM systems; (f) Thermal cycling stability of the CGP-*R*2/PPDMS composite material at a heating power of 30 W.

markedly lower than that of the TFLEX-700 thermal pad (82 K·mm^2·W^{-1}). This lower R_c can be attributed to the corrugated structure of the thermal filler, low compressive modulus of PPDMS, and strong interfacial interactions between both components. Therefore, CGP-*R*2/PPDMS with low compressive modulus is easier to fill and adapt to the microgaps between the assembly surfaces, resulting in a larger microcontact area and a lower R_c.[43,44] Combining high through-plane thermal conductivity and low R_c, the finite element analysis shown in Fig. 5(e) confirms the excellent heat dissipation performance of our TIM samples. Furthermore, we conducted cyclic thermal shock testing using CGP-*R*2/PPDMS as the TIM by controlling the on/off operation of the heater at a rated power of 30 W. The shown results in Fig. 5(f) demonstrate the highly stable heat-dissipation performance of CGP-*R*2/PPDMS during continuous heating/cooling shocks of the device over 30000 s.

Next, we conducted practical tests on real TIMs applied to cool computer CPUs to demonstrate the superior heat dissipation performance of CGP-*R*2/PPDMS compared with that of TFLEX-700 thermal pads. The testing setup and photographs are shown in Figs. 6(a) and 6(b), respectively. In this test, we directly physically mounted CGP-*R*2/PPDMS and TFLEX-700 with the same area and BLT between the CPU (Intel Core E2180, 2000 MHz) and aluminum heat sink by applying vertical package pressure using spring screws. The CPU was fixed to the motherboard, and the heat sink was connected to a cooling fan using screws to transfer heat to the flowing air. We used professional system diagnostic software (AIDA64) to operate the CPU under maximum heating conditions and recorded the CPU core temperature. The results shown in Fig. 6(c) demonstrate that when using CGP-*R*2/PPDMS as a TIM, the temperature rise rate of the CPU core is slower than when using TFLEX-700, and a lower temperature is consistently maintained (*e.g.*, at 300 s, ΔT=9.0 °C). The temperature comparison curve of the computer motherboard in Fig. 6(d) also

https://doi.org/10.1007/s10118-024-3159-8

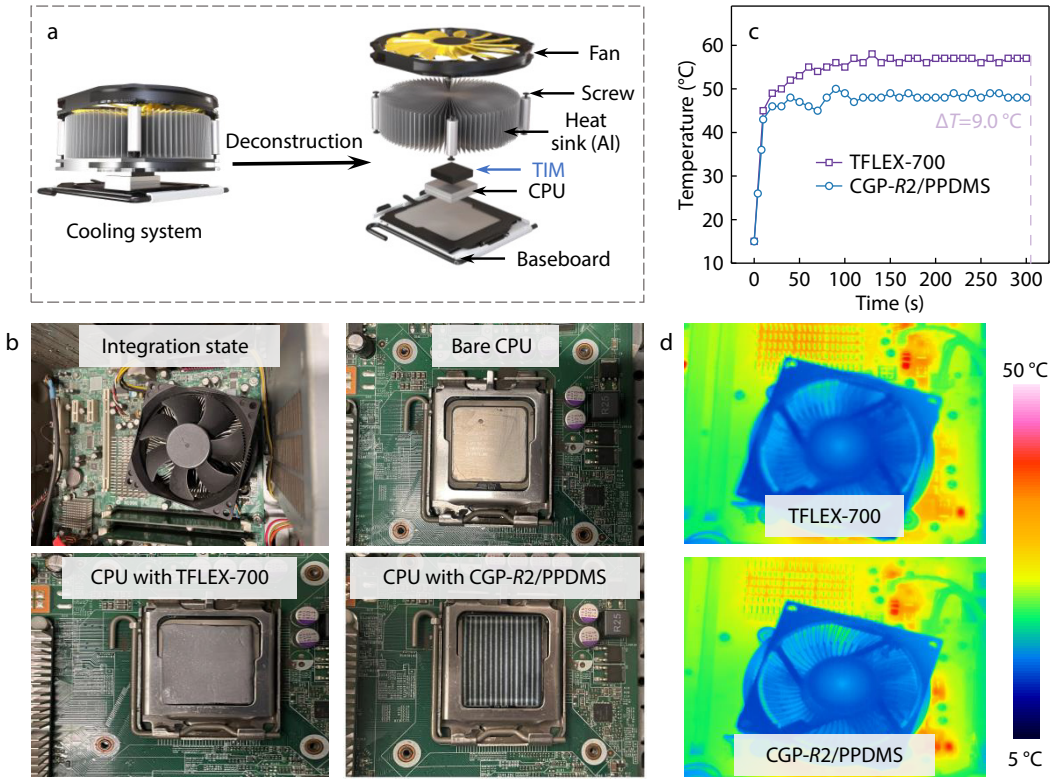

Fig. 6 Application of CGP-*R*2/PPDMS in CPU cooling. (a) Schematic comparing the cooling efficiency of CGP-*R*2/PPDMS and TFLEX-700 thermal pads; (b) Photographs of the setup; (c) Variation of the CPU temperature with operating time; (d) Thermal infrared images of the motherboard when using TFLEX-700 and CGP-*R*2/PPDMS as TIMs, respectively.

shows lower temperatures when using CGP-*R*2/PPDMS as a TIM. These results indicate that CGP-*R*2/PPDMS has the potential to be used in real electronic cooling applications and as an advanced replacement for thermal pads.

CONCLUSIONS

By functionalizing the surface of graphene films and employing a convenient and applicable method for large-scale fabrication, we successfully prepared CGP/PPDMS composite materials with a unique corrugated structure for thermal fillers. This synthesis strategy is based on the hydrosilylation reaction to form chemical bonds between the organosilicon matrix and fillers, resulting in composite materials with a low compressive modulus and high resilience. The CGP-*R*2/PPDMS composite material demonstrates excellent flexibility, elasticity, and high thermal conductivity. Specifically, the composite material possesses high thermal conductivity ($\kappa_{\perp}$=14.4 W·m^{-1}·K^{-1} and $\kappa_{\parallel}$=130 W·m^{-1}·K^{-1}) and low contact thermal resistance (R_c=52.7 K·mm^2·W^{-1} at 0.1 MPa). Additionally, owing to the high deformability, soft elasticity, and low compressive modulus of PPDMS, CGP-*R*2/PPDMS can withstand up to 20% elastic strain and exhibit a low compressive modulus of 143 kPa. Furthermore, the TCE reaches 831% for a filler loading of 1 wt%. In the TIM performance test, the CGP-*R*2/PPDMS composite material demonstrates not only outstanding cooling efficiency (38.2% improvement compared with commercial TIM TFLEX-700) but also highly efficient and stable interfacial heat dissipation performance under actual CPU full-load operating conditions (the CPU temperature decreased by 9.0 °C compared with the TFLEX-700 heat dissipation system). Overall, by optimizing the interface state between fillers and matrix, we successfully developed a CGP/PPDMS composite material with a unique corrugated structure, providing a simple and innovative approach to address the trade-off between low modulus and high thermal conductivity in materials, while maintaining excellent stability and competitive advantages for high-performance TIMs

Conflict of Interests

The authors declare no interest conflict.

Electronic Supplementary Information

Electronic supplementary information (ESI) is available free of charge in the online version of this article at http://doi.org/10.1007/s10118-024-3159-8.

Data Availability Statement

The data that support the findings of this study are available from the corresponding author upon reasonable request. The authors' contact information: qmm@tju.edu.cn (M.M.Q.), weifeng@tju.edu.cn (W.F.).

ACKNOWLEDGMENTS

This work was financially supported by the National Natural Science Foundation of China (Nos. 52130303, 52327802 and 52173078) and National Key R&D Program of China (No. 2022YFB3805702).

REFERENCES

1 Zhang, Q.; Lv, Y.; Wang, Y.; Yu, S.; Li, C.; Ma, R.; Chen, Y. Temperature-dependent dual-mode thermal management device with net zero energy for year-round energy saving. *Nat. Commun.* **2022**, *13*, 4874.
2 Zhu, Z.; Li, C.; Songfeng, E.; Xie, L.; Geng, R.; Lin, C.-T.; Li, L.; Yao, Y. Enhanced thermal conductivity of polyurethane composites *via* engineering small/large sizes interconnected boron nitride nanosheets. *Compos. Sci. Technol.* **2019**, *170*, 93–100.
3 Peng, L.; Yu, H.; Chen, C.; He, Q.; Zhang, H.; Zhao, F.; Qin, M.; Feng, Y.; Feng, W. Tailoring dense, orientation-tunable, and interleavedly structured carbon-based heat dissipation plates. *Adv. Sci.* **2023**, 2205962.
4 Yue, J.; Feng, Y.; Qin, M.; Feng, W. Carbon-based materials with combined functions of thermal management and electromagnetic protection: preparation, mechanisms, properties, and applications. *Nano Res.* **2024**, *17*, 883–903.
5 Yu, C.; Zhang, J.; Li, Z.; Tian, W.; Wang, L.; Luo, J.; Li, Q.; Fan, X.; Yao, Y. Enhanced through-plane thermal conductivity of boron nitride/epoxy composites. *Compos. Part Appl. Sci. Manuf.* **2017**, *98*, 25–31.
6 Xu, X.; Chen, J.; Zhou, J.; Li, B. Thermal conductivity of polymers and their nanocomposites. *Adv. Mater.* **2018**, *30*, 1705544.
7 Yu, C.; Gong, W.; Tian, W.; Zhang, Q.; Xu, Y.; Lin, Z.; Hu, M.; Fan, X.; Yao, Y. Hot-pressing induced alignment of boron nitride in polyurethane for composite films with thermal conductivity over 50 W m^{-1} K^{-1}. *Compos. Sci. Technol.* **2018**, *160*, 199–207.
8 Balandin, A. A.; Ghosh, S.; Bao, W.; Calizo, I.; Teweldebrhan, D.; Miao, F.; Lau, C. N. Superior thermal conductivity of single-layer graphene. *Nano Lett.* **2008**, *8*, 902–907.
9 Zhang, J.; Shi, G.; Jiang, C.; Ju, S.; Jiang, D. 3D bridged carbon nanoring/graphene hybrid paper as a high-performance lateral heat spreader. *Small* **2015**, *11*, 6197–6204.
10 Kong, Q.; Liu, Z.; Gao, J.; Chen, C.; Zhang, Q.; Zhou, G.; Tao, Z.; Zhang, X.; Wang, M.; Li, F.; Cai, R. Hierarchical graphene-carbon fiber composite paper as a flexible lateral heat spreader. *Adv. Funct. Mater.* **2014**, *24*, 4222–4228.
11 Ying, J.; Tan, X.; Lv, L.; Wang, X.; Gao, J.; Yan, Q.; Ma, H.; Nishimura, K.; Li, H.; Yu, J.; Liu, T.-H.; Xiang, R.; Sun, R.; Jiang, N.; Wong, C.; Maruyama, S.; Lin, C. T.; Dai, W. Tailoring highly ordered graphene framework in epoxy for high-performance polymer-based heat dissipation plates. *ACS Nano* **2021**, *15*, 12922–12934.
12 Song, S. H.; Park, K. H.; Kim, B. H.; Choi, Y. W.; Jun, G. H.; Lee, D. J.; Kong, B. S.; Paik, K. W.; Jeon, S. Enhanced thermal conductivity of epoxy-graphene composites by using non-oxidized graphene flakes with non-covalent functionalization. *Adv. Mater.* **2013**, *25*, 732–737.
13 Shtein, M.; Nadiv, R.; Buzaglo, M.; Kahil, K.; Regev, O. Thermally conductive graphene-polymer composites: size, percolation, and synergy effects. *Chem. Mater.* **2015**, *27*, 2100–2106.
14 Wang, F.; Zeng, X.; Yao, Y.; Sun, R.; Xu, J.; Wong, C. P. Silver nanoparticle-deposited boron nitride nanosheets as fillers for polymeric composites with high thermal conductivity. *Sci. Rep.* **2016**, *6*, 19394.
15 Ma, J.; Shang, T.; Ren, L.; Yao, Y.; Zhang, T.; Xie, J.; Zhang, B.; Zeng, X.; Sun, R.; Xu, J. B.; Wong, C. P. Through-plane assembly of carbon fibers into 3D skeleton achieving enhanced thermal conductivity of a thermal interface material. *Chem. Eng. J.* **2020**, *380*, 122550.
16 Hou, H.; Dai, W.; Yan, Q.; Lv, L.; Alam, F. E.; Yang, M.; Yao, Y.; Zeng, X.; Xu, J.-B.; Yu, J.; Jiang, N.; Lin, C. T. Graphene size-dependent modulation of graphene frameworks contributing to the superior thermal conductivity of epoxy composites. *J. Mater. Chem. A* **2018**, *6*, 12091–12097.
17 Yang, J.; Zhang, E.; Li, X.; Zhang, Y.; Qu, J.; Yu, Z. Z. Cellulose/graphene aerogel supported phase change composites with high thermal conductivity and good shape stability for thermal energy storage. *Carbon* **2016**, *98*, 50–57.
18 Qin, M.; Xu, Y.; Cao, R.; Feng, W.; Chen, L. Efficiently controlling the 3D thermal conductivity of a polymer nanocomposite *via* a hyperelastic double-continuous network of graphene and sponge. *Adv. Funct. Mater.* **2018**, *28*, 1805053.
19 Ji, H.; Sellan, D. P.; Pettes, M. T.; Kong, X.; Ji, J.; Shi, L.; Ruoff, R. S. Enhanced thermal conductivity of phase change materials with ultrathin-graphite foams for thermal energy storage. *Energy Environ. Sci.* **2014**, *7*, 1185–1192.
20 Yang, J.; Li, X.; Han, S.; Yang, R.; Min, P.; Yu, Z. Z. High-quality graphene aerogels for thermally conductive phase change composites with excellent shape stability. *J. Mater. Chem. A* **2018**, *6*, 5880–5886.
21 He, Q.; Qin, M.; Zhang, H.; Yue, J.; Peng, L.; Liu, G.; Feng, Y.; Feng, W. Patterned liquid metal embedded in brush-shaped polymers for dynamic thermal management. *Mater. Horiz.* **2023**, *2*, 531–544.
22 Gao, W.; Wang, M.; Bai, H. A review of multifunctional nacre-mimetic materials based on bidirectional freeze casting. *J. Mech. Behav. Biomed. Mater.* **2020**, *109*, 103820.
23 Min, P.; Liu, J.; Li, X.; An, F.; Liu, P.; Shen, Y.; Koratkar, N.; Yu, Z. Thermally conductive phase change composites featuring anisotropic graphene aerogels for real-time and fast-charging solar-thermal energy conversion. *Adv. Funct. Mater.* **2018**, *28*, 1805365.
24 Li, J.; Zhang, Y.; Liang, T.; Bai, X.; Pang, Y.; Zeng, X.; Hu, Q.; Tu, W.; Ye, Z.; Du, G.; Sun, R.; Zeng, X. Thermal interface materials with both high through-plane thermal conductivity and excellent elastic compliance. *Chem. Mater.* **2021**, *33*, 8926–8937.
25 Dai, W.; Ma, T.; Yan, Q.; Gao, J.; Tan, X.; Lv, L.; Hou, H.; Wei, Q.; Yu, J.; Wu, J.; Yao, Y.; Du, S.; Sun, R.; Jiang, N.; Wang, Y.; Kong, J.; Wong, C.; Maruyama, S.; Lin, C. T. Metal-level thermally conductive yet soft graphene thermal interface materials. *ACS Nano* **2019**, *13*, 11561–11571.
26 Tang, L.; Ruan, K.; Liu, X.; Tang, Y.; Zhang, Y.; Gu, J. Flexible and robust functionalized boron nitride/poly(p-phenylene benzobisoxazole) nanocomposite paper with high thermal conductivity and outstanding electrical insulation. *Nano-Micro Lett.* **2024**, *16*, 38.
27 Zhang, Y.; Choi, J. R.; Park, S. J. Enhancing the heat and load transfer efficiency by optimizing the interface of hexagonal boron nitride/elastomer nanocomposites for thermal management applications. *Polymer* **2018**, *143*, 1–9.
28 Chu, K.; Wang, J.; Liu, Y.; Geng, Z. Graphene defect engineering for optimizing the interface and mechanical properties of graphene/copper composites. *Carbon* **2018**, *140*, 112–123.
29 Hu, P.; Madsen, J.; Skov, A. L. One reaction to make highly stretchable or extremely soft silicone elastomers from easily available materials. *Nat. Commun.* **2022**, *13*, 370.
30 Peng, L.; Xu, Z.; Liu, Z.; Guo, Y.; Li, P.; Gao, C. Ultrahigh thermal conductive yet superflexible graphene films. *Adv. Mater.* **2017**, *29*, 1700589.
31 Gao, X.; Zheng, L.; Luo, F.; Qian, J.; Wang, J.; Yan, M.; Wang, W.; Wu, Q.; Tang, J.; Cao, Y.; Tan, C.; Tang, J.; Zhu, M.; Wang, Y.; Li, Y.; Sun, L.; Gao, G.; Yin, J.; Lin, L.; Liu, Z.; Qin, S.; Peng, H. Integrated

wafer-scale ultra-flat graphene by gradient surface energy modulation. *Nat. Commun.* **2022**, *13*, 5410.
32 Srinivasan, N. R.; Shankar, P. A.; Bandyopadhyaya, R. Plasma treated activated carbon impregnated with silver nanoparticles for improved antibacterial effect in water disinfection. *Carbon* **2013**, *57*, 1–10.
33 Kang, S.; He, M.; Chen, M.; Wang, J.; Zheng, L.; Chang, X.; Duan, H.; Sun, D.; Dong, M.; Cui, L. Ultrafast plasma immersion strategy for rational modulation of oxygen-containing and amino groups in graphitic carbon nitride. *Carbon* **2020**, *159*, 51–64.
34 Han, X.; Gao, J.; Chen, T.; Zhao, Y. Interfacial interaction and steric repulsion in polymer-assisted liquid exfoliation to produce high-quality graphene. *Chem. Pap.* **2020**, *74*, 757–765.
35 Lin, S. B.; Durfee, L. D.; Ekeland, R. A.; McVie, J.; Schalau, G. K. Recent advances in silicone pressure-sensitive adhesives. *J. Adhes. Sci. Technol.* **2007**, *21*, 605–623.
36 Witte, P. T.; Boland, S.; Kirby, F.; van Maanen, R.; Bleeker, B. F.; de Winter, D. A. M.; Post, J. A.; Geus, J. W.; Berben, P. H. NanoSelect Pd catalysts: what causes the high selectivity of these supported colloidal catalysts in alkyne semi-hydrogenation. *ChemCatChem.* **2013**, *5*, 582–587.
37 Wang, B.; Ma, H. W.; Shen, K. H.; Jun, D.; Li, Y. Synthesis and characterization of in-chain silyl-hydride functional SBR and self-crosslinking elastomer. *Chin. Chem. Lett.* **2012**, *23*, 1419–1422.
38 Ni, Y.; Yang, D.; Wei, Q.; Yu, L.; Ai, J.; Zhang, L. Plasticizer-induced enhanced electromechanical performance of natural rubber dielectric elastomer composites. *Compos. Sci. Technol.* **2020**, *195*, 108202.
39 Liu, J.; Fang, Z.; An, J.; Bao, C. Effect of the cross-linking of polyorganosiloxane on highly thermally conductive silicone rubber's mechanical, dielectric, and thermally conductive properties and thermal reliability. *Compos. Commun.* **2024**, *45*, 101781.
40 Zhong, X.; He, M.; Zhang, C.; Guo, Y.; Hu, J.; Gu, J. Heterostructured BN@Co-C@C endowing polyester composites excellent thermal conductivity and microwave absorption at C band. *Adv. Funct. Mater.* **2024**, 2313544.
41 Yu, H.; Chen, C.; Sun, J.; Zhang, H.; Feng, Y.; Qin, M.; Feng, W. Highly thermally conductive polymer/graphene composites with rapid room-temperature self-healing capacity. *Nano-Micro Lett.* **2022**, *14*, 135.
42 Gong, J.; Tan, X.; Yuan, Q.; Liu, Z.; Ying, J.; Lv, L.; Yan, Q.; Chu, W.; Xue, C.; Yu, J.; Nishimura, K.; Jiang, N.; Lin, C.; Dai, W. A spiral graphene framework containing highly ordered graphene microtubes for polymer composites with superior through-plane thermal conductivity. *Chin. J. Chem.* **2022**, *40*, 329–336.
43 Yin, W.; Qin, M.; Yu, H.; Sun, J.; Feng, W. Hyperelastic graphene aerogels reinforced by in-suit welding polyimide nano fiber with leaf skeleton structure and adjustable thermal conductivity for morphology and temperature sensing. *Adv. Fiber Mater.* **2023**, *5*, 1037–1049.
44 Wang, S. S.; Feng, D. Y.; Zhang, Z. M.; Liu, X.; Ruan, K. P.; Guo, Y. Q.; Gu, J. W. Highly thermally conductive polydimethylsiloxane composites with controllable 3D GO@f-CNTs networks *via* self-sacrificing template method. *Chinese J. Polym. Sci.* **2024**, *42*, 897–906.

https://doi.org/10.1007/s10118-024-3159-8